Received: 9 January 2019 | Revised: 28 May 2019 | Accepted: 29 May 2019

DOI: 10.1002/jbio.201900008

FULL ARTICLE

JOURNAL OF BIOPHOTONICS

A deep learning based pipeline for optical coherence tomography angiography

Xi Liu[1] | Zhiyu Huang[1] | Zhenzhou Wang[2] | Chenyao Wen[1] | Zhe Jiang[1] | Zekuan Yu[1] | Jingfeng Liu[2] | Gangjun Liu[3] | Xiaolin Huang[4] | Andreas Maier[5] | Qiushi Ren[1,3] | Yanye Lu[5]*

[1]Department of Biomedical Engineering, College of Engineering, Peking University, Beijing, China

[2]Department of Emergency Medicine, Beijing Friendship Hospital, Capital Medical University, Beijing, China

[3]Shenzhen Graduate School, Peking University, Shenzhen, China

[4]Institute of Image Processing and Pattern Recognition, Institute of Medical Robotics, Shanghai Jiao Tong University, Shanghai, China

[5]Pattern Recognition Lab, Department of Computer Science, Friedrich-Alexander-University Erlangen-Nuremberg, Erlangen, Germany

***Correspondence**
Yanye Lu, Pattern Recognition Lab, Department of Computer Science, Friedrich-Alexander-University Erlangen-Nuremberg, Martensstr. 3, 91058 Erlangen, Germany.
Email: yanye.lu@pku.edu.cn

Funding information
National Key Instrumentation Development Project of China, Grant/Award Number: 2013YQ030651; National Natural Science Foundation of China, Grant/Award Number: 81421004

Abstract

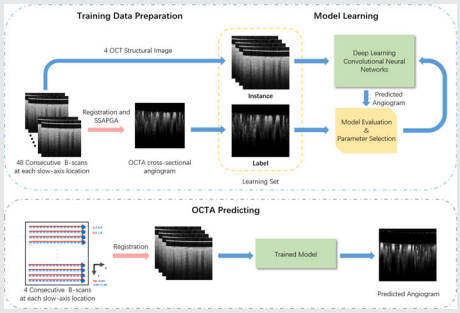

Optical coherence tomography angiography (OCTA) is a relatively new imaging modality that generates microvasculature map. Meanwhile, deep learning has been recently attracting considerable attention in image-to-image translation, such as image denoising, super-resolution and prediction. In this paper, we propose a deep learning based pipeline for OCTA. This pipeline consists of three parts: training data preparation, model learning and OCTA predicting using the trained model. To be mentioned, the datasets used in this work were automatically generated by a conventional system setup without any expert labeling. Promising results have been validated by in-vivo animal experiments, which demonstrate that deep learning is able to outperform traditional OCTA methods. The image quality is improved in not only higher signal-to-noise ratio but also better vasculature connectivity by laser speckle eliminating, showing potential in clinical use. Schematic description of the deep learning based optical coherent tomography angiography pipeline.

KEYWORDS
CNN, deep learning, OCT angiography

1 | INTRODUCTION

Over the past two decades, optical coherent tomography (OCT) has become one of the most important imaging modalities in healthcare, which is noninvasive and depth-resolved [1–3]. OCT is able to generate in-vivo structural images by detecting interference signal between the reflected signal from reference mirror and the backscattering signals from biological tissue [3, 4]. Nowadays, OCT is widely applied to neurology, ophthalmology, dermatology, gastroenterology and cardiology by virtue of its excellent sectioning ability [5–11]. In addition to structural imaging, OCT has been explored and extended for functional imaging with the rapid development of light source and detection techniques, for instance, optical coherence tomography based angiography (OCTA) [12–16].

Compared with traditional angiographic techniques (ie, fluorescein), OCTA is no-injection and dye-free. A large

number of algorithms have been investigated to contrast blood vessels from static tissue by assessing the change in OCT signal caused by red blood cells (RBCs). Essentially, according to the information employed by the OCTA algorithms, OCTA methods can be classified into three categories: phase-signal-based OCTA techniques, intensity-signal-based OCTA techniques and complex-signal-based OCTA techniques [17, 18]. As of now, all of the methods are based on measurement of OCT signal change between adjacent B-scans at the same location. For a certain position, the flow intensity is calculated from phase variance or intensity variance using different statistical methods. However, both of them can only utilize partial information of OCT signal change due to the limitations of analytical methods. Besides, OCTA image contains a wealth of morphological information, which has never been utilized in prior studies. Unlike analytical methods [19–28], learning based solutions, such as deep learning, are able to mine as much inner connection hidden in OCT signal as possible, even the concealed morphological information.

Dramatic improvements in parallel computing techniques make it possible to process large amounts of data in deep neural networks. Recent breakthroughs in deep learning are mainly originated from deep convolutional neural networks (CNNs) [29–33]. In medical imaging field, a large number of deep learning models have been developed for image enhancement and image reconstruction. Recently, Lee et al [34] reported an attempt on generating retinal flow maps from structural OCT with an U-shaped auto-encoder network. Although they have employed large amount of clinical data for model training, but the result is not quite satisfactory and the deep learning model is unable to identify small size vessels correctly. Structural information of small size vessels is difficult to distinguish from OCT noise due to the strong light scattering in tissue. Besides, the labeling quality in [34] is limited to generate promising models. Note that, the image quality of label for model training is crucial, which could greatly influence the angiography ability of trained model.

In this work, we propose a novel deep learning based pipeline as an alternative to conventional analytic OCTA algorithms. The pipeline employs a CNN-based end-to-end neural network for OCTA, which is capable of mapping microvasculature with better image contrast and signal-to-noise ratio (SNR) comparing to existing algorithms. Particularly, vascular connectivity is also improved by laser speckle eliminating. In order to acquire high quality labels for training, we designed an in-vivo animal imaging protocol. The proposed method is validated through the in-vivo animal experiments and angiography results are compared with convolutional methods both in cross-sectional and enface perspective.

2 | MATERIALS AND METHODS

2.1 | OCTA techniques

OCT technique is able to generate cross-sectional (2D) and three-dimensional (3D) images of live tissue that contain structural information deriving from depth-resolved tissue reflectivity. In the mid-1990s, great efforts were made for blood flow measurement following the invention of OCT. The Doppler principle was firstly utilized in the analysis of the backscattered OCT signal which demonstrates promising results [35–37]. This very first idea is based on the assumption that flowing RBCs will cause a frequency or phase shift Δf_D on OCT signal. This minor change can be acquired through OCT signal demodulating and the blood flow velocity v_{RBC} can be calculated by the following equation

$$v_{RBC} = \frac{\lambda}{2n \cdot \cos\theta} \cdot \Delta f_D \tag{1}$$

where λ is the central wavelength of incident beam, n is the refractive index of surrounding tissue and θ is the enclosed angle between incident beam and flow direction. Although Doppler OCT is able to visualize and quantify blood velocity in larger vessels, it is still inadequate for clinical use.

Recently, a new technique named OCT-based angiography has been invented based on the variations of OCT signals. While the blood is flowing, the moving RBCs can be considered as an intrinsic contrast agent that causes OCT signal changing over time, in the meanwhile, the OCT signal of surrounding biological tissue keeps steady. Several analytic algorithms have been developed through calculating the differences in OCT signals acquired at the same location with short time sequence. OCT signal is consisted of amplitude and phase information, which can be written as a complex function at lateral x, axial location z and time t in a B-scan:

$$C(x,z,t) = A(x,z,t) \cdot e^{i \cdot \Phi(x,z,t)} \tag{2}$$

where A indicates the signal amplitude and Φ is the phase component. For now, OCTA methods can be classified based on what information they used and whether they used full-spectrum or split-spectrum processing [19–27].

The split-spectrum amplitude and phase-gradient angiography (SSAPGA) algorithm, which is recently proposed by Liu et al [38], employs both amplitude parts and phase parts to calculate and distinguish blood flow from static tissue. This algorithm extracts the phase shift induced by RBC movement ($\Delta\varphi_v$) from total phase difference ($\Delta\varphi_E$) to eliminate the false phase difference induced by bulk motion ($\Delta\varphi_\alpha$) and phase noise ($\Delta\varphi_n$). Eventually, the flow signal

calculated based on phase-gradient angiography (PGA) method could be simplified as the following equation:

$$Flow_{PGA}(x,z) = \frac{d(\Delta\varphi_E(x,z))}{dz} \approx \frac{d(\Delta\varphi_v(x,z))}{dz} \quad (3)$$

After combining amplitude and split-spectrum, the SSAPGA algorithm demonstrates superior performance in OCTA [17, 18, 38]. Therefore, we applied this OCTA method to generate label data set, which would be further explained in the following sections.

For comparison, another two OCTA methods were used, namely as correlation mapping (CM) and power intensity differential (PID). The former is based on intensity correlation [26] and the latter is based on squared intensity difference [27].

2.2 | Deep learning based OCTA pipeline

In this work, we propose a deep learning based pipeline for OCTA, which treats OCTA as an end-to-end image translation task. This pipeline consists of three parts: training data preparation, model learning and OCTA predicting using the trained model. Figure 1 shows the schematic description of the proposed pipeline.

2.2.1 | Training data set

For supervised deep network training, input pairs of original structural images and ground truth label images are required. Generally, the ground truth is labeled by experts according to their prior knowledge, but it is time-consuming and unachievable in OCT angiography. In 2010, Mariampillai et al found that the number of repeated B-scans has a great impact on OCT angiography SNR [39]. Therefore, we captured 48 consecutive B-scans at each slow-axis location and applied SSAPGA to generate label angiograms as the ground truth that owns much higher SNR and less speckle noise (shown as bright and dark dots in the image). To be mentioned, all of the 48 consecutive B-scans at each slow-axis location are registered by rigid registration algorithm [40]. We randomly extracted four of the registered OCT structural B-Scan images as the input of deepCNN.

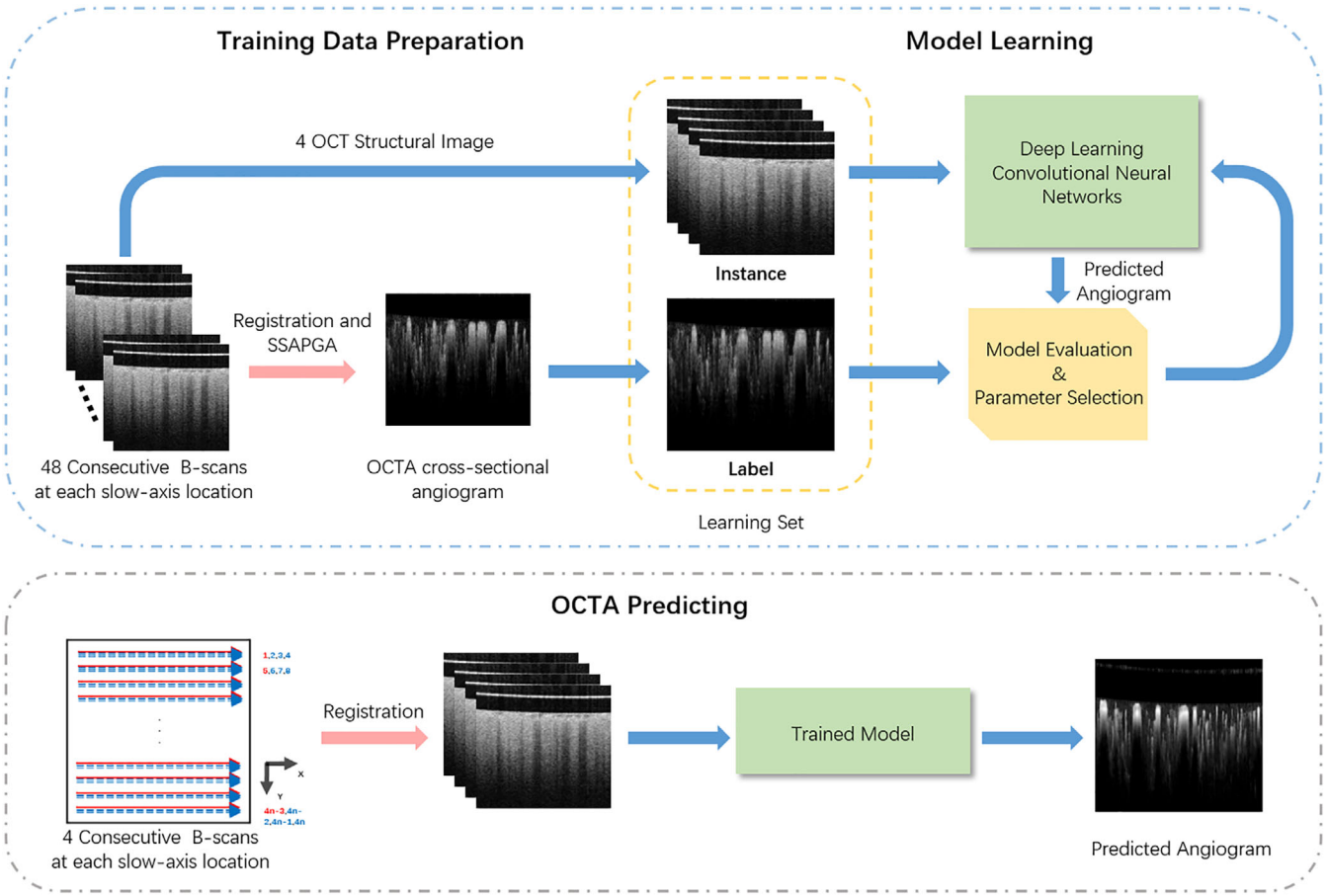

FIGURE 1 Schematic description of the deep learning based optical coherence tomography angiography pipeline

2.2.2 | Overview of CNN

Convolutional neural network (CNN) is a specialized kind of neural network for data processing [41]. It is based on the convolution operation, which is an operation on two functions of a real-valued argument. CNN has achieved tremendously success in various practical applications in different spatial dimensions and even in time dimension.

Generally, model training is consisted of forward propagation, cost function calculation and back propagation. First, we use a feedforward neural network to accept an input x and produce an output $\hat{y}$, information flows forward through the network until it produces a scalar cost $J(\theta)$ through the designed cost function. Then, back propagation algorithm transmits the cost value back to the network through chain rules, computing the gradient and modifies the weights of the network.

Recently, driven by the easy access to large-scale dataset and the enormous potential of deep learning, great progresses were achieved to help train the CNN models effectively, including ReLU [42], tradeoff between depth and width [43], dropout [44], parameter initialization [45], Adam optimization algorithms [46] and batch normalization [47].

2.2.3 | Model evaluation and parameter selection

During training, it is necessary to evaluate the model performance to facilitate finding appropriate hyper parameters of the model. For a quantitative assessment, we used additional cross-sectional image pairs as validation set and calculated the peak signal-to-noise ratio (PSNR) value, which is defined as:

$$PSNR = 10 \cdot \log_{10}\left(\frac{MAX_G^2}{MSE}\right) \tag{4}$$

where G is the label image, MAX_G is the maximum value of image G and MSE is the mean square error between G and the output image.

2.3 | Experimental setup

2.3.1 | System setup and imaging protocol

For this study, a Spectral Domain OCT with typical configuration has been built, as shown in Figure 2. Briefly, the light source is a wideband super luminescent diode with a central wavelength of 845 nm and a full width at half maximum bandwidth of 30 nm, offering a theoretical high axial resolution of approximately 10 μm. The light power exposure at rat brain surface is 2.4 mW. Besides, the measured lateral resolution is approximately 12 μm. A high-speed spectrometer fitted out a fast line scan charge-coupled device (CCD) camera with a 28 kHz line scan rate was used as the detection unit in our system.

In each volumetric scan, the field of view was 2.5 × 2.5 mm and the imaging depth was about 1 mm. Each B-scan was formed by 360 A-lines and a total 300 slow-axis locations were sampled to generate a 3D OCTA volume. In order to acquire vascular signal label with high contrast for training, we captured 48 consecutive B-scans at each slow-axis location.

2.3.2 | Animal preparation

A total of four Sprague Dawley rats of 8-9 weeks' old were used in our animal experiments. Intraperitoneal injection of 10% chloral hydrate (4 mLkg) was performed before

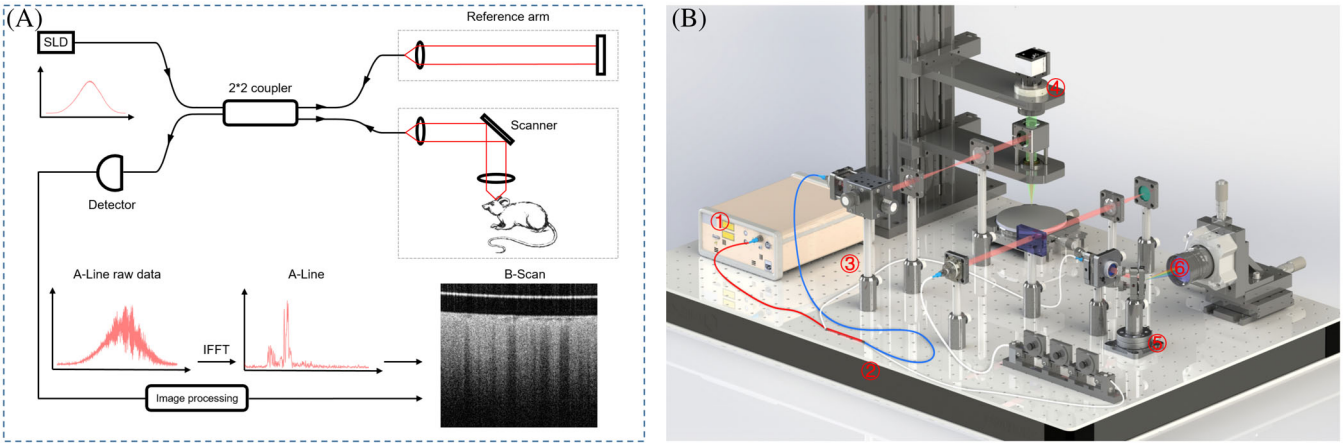

FIGURE 2 Spectral Domain OCT (SD-OCT) system in this study. A, Schematic diagram of the SD-OCT system. B, 3D rendering of the SD-OCT coupled with a digital camera for visual guidance. ① super luminescent diode, ② 50:50 coupler, ③ galvanometer, ④ digital camera, ⑤ grating, ⑥ line scan CCD camera

beginning all surgical procedures. The rat head was fixed in a stereotaxic frame, and the scalp is retracted. The skull was thinned with a high-speed dental drill to generate a window of 4 mm × 4 mm area. After craniotomy, the dura mater was quickly removed with fine forceps. A square piece of cover glass was placed on the exposed brain tissue, and the edge was immediately glued onto the skull using dental resin. During imaging, rats were first anesthetized in an induction chamber with 3.0% isoflurane and then maintained with 1.3% isoflurane. All animal procedures were reviewed and approved by the Subcommittee on Research Animal Care at Beijing Friendship Hospital, where these experiments were performed.

2.3.3 | Network structures

Our pipeline employed a deep CNNwith depth a D_l consists of three types of layers, as shown in Figure 3. This CNN architecture is modified from a single channel input CNN for image denoising [31]. More specifically, the multi-channel inputs of our network were four OCT structural images. The first layer consists of 64 feature maps generated by 64 filters (size $= 3 \times 3 \times 4$) and connected with ReLU for nonlinearity. As for layer block 2 to layer block ($D_l - 1$), each layer was convoluted by 64 filters of size $3 \times 3 \times 64$, and connects with batch normalization [47] and ReLU [42] for faster convergence. The last layer used 1 filter (size $= 3 \times 3 \times 64$) to generate the output.

In the architecture design, we found the network depth has a great impact on the tradeoff between performance and efficiency. It has been pointed out that the receptive field is correlated with depth D_l [48], which should be calculated as $(2D_l + 1) \times (2D_l + 1)$ in our CNN model. A larger receptive field is able to make better use of relevant information in the field. Additionally, patch-based image processing techniques commonly use a 40×40 patch, which contains sufficient image information to learn. Therefore, in consideration of graphics processing unit (GPU) performance and the receptive field size of CNNs, we set the D_l value as 20 and extracted image patch size of 40×40.

2.3.4 | Implementation details

Network training is performed by minimizing the mean squared error (MSE) loss between the generated OCTA cross-sectional angiogram and label image. We adopted the Adam gradient-based optimization algorithm for minimization of the cost function [46], and the epoch was set to 50. The convolution kernel weights were initialized using random Gaussian distributions with a weight decay of 0.001 and a mini-batch size of 128.

3 | RESULTS AND DISCUSSION

In order to train CNN models for OCTA, a total of six data volumes were obtained from four rats with 48 consecutive B-scans at each slow-axis location as a result of 1800 cross-sectional training pairs. Each training pair consists of four randomly selected structural OCT images and one label angiogram generated by SSAGPA method. We used 5 of the 6 volumes as training data and the remaining 1 volume as testing data.

The OCTA cross-sectional angiogram generated from 48 consecutive B-scans and four consecutive B-scans using different methods are shown in Figure 4A-E. Obviously, the SNR of Figure 4A is much better and have less speckle noise. This is the reason that we designated angiograms from 48 consecutive B-scans as the "ground truth of the dataset."

The CNN model is trained with 194 000 iterations and periodically assessed against the validation set. The training time is 10 hours using parallelized training across a NVIDIA Titan XP GPU. Figure 4C shows an example CNN output from four consecutive B-scans. Compared with the other methods, CNN method can eliminate speckle noise to a certain extent and enhance the blood flow signal. This is due to the powerful modeling capability of deep neural network,

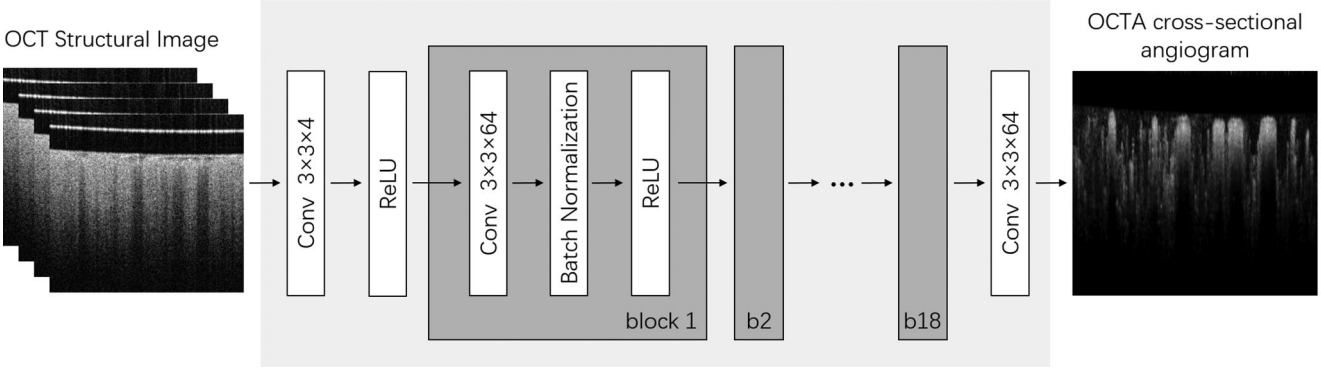

FIGURE 3 Architecture of the deep learning network in this study

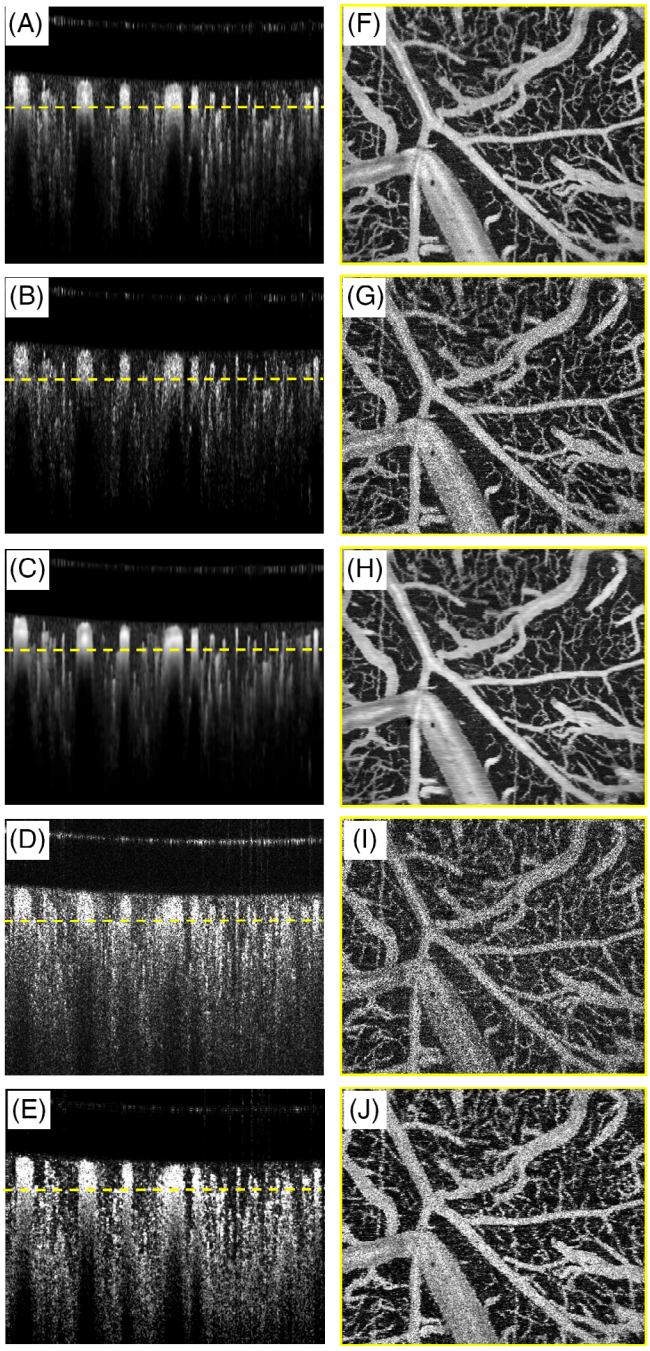

FIGURE 4 Example cross-sectional optical coherence tomography angiography angiogram generated from (A) 48 consecutive B-scans using split-spectrum amplitude and phase-gradient angiography (SSAPGA), (B-E) four consecutive B-scans using SSAPGA, convolutional neural network, power intensity differential and correlation mapping respectively. F-J, Enface OCTA angiograms at the representative depth position (marked with yellow dotted line) of each method and protocol

which is able to mine more intrinsic connections from OCT signals. Enface OCTA angiograms at the representative depth position (marked with yellow dotted line) of each method and protocol are shown in Figure 4F-J. It can be seen that, under the same scanning protocol, the CNN-angiogram has better image quality and better continuity of vasculature. To be mentioned, all the enface OCTA angiograms are processed by normalization and outlier elimination (4%) without any contrast adjustment. This method aims to relieve the human visual change of OCTA angiogram induced by speckle noise, which is in the form of ultra-bright dots in the image. Specifically, we eliminated the noise by histogram thresholding.

The performance of different methods was also compared in enface view, which is the preferred way to evaluate vasculatures. Figure 5 shows the maximum intensity projection (MIP) images using different methods and scanning protocols. Figure 5A is the result of SSAPGA with protocol of 48 consecutive scans at each slow-axis location, which owns great image quality and presents more details of vasculature. Figure 5B-E are the results of SSAPGA, CNN, PID and CM methods with the same protocol (four consecutive scans at each slow-axis location), respectively. Such protocol is commonly used in OCTA devices. One section of detailed enface OCTA angiogram is selected and marked with yellow dotted line. The corresponding enlarged images are shown in Figure 5F-J. Compared to other methods, microvessel network pointed by red arrow from CNN method presents better SNR and the vascular network is more clear and distinct. The vessel pointed by brown arrow from CNN method has a great uniformity because the speckle noise is totally smoothed. We speculate this effect to the MSE loss function used in CNN network training procedure. However, it would potentially generate blurry cross-sectional OCTA angiogram and cause loss of details (Figure 4C) which can further cause distortion at enface angiogram (marked by green dotted circle in Figure 5H).

For further investigation, we decreased the number of CNN input channels, since the OCTA technology is suffering from imaging speed, which is caused by limitation of detector. In this work, 3-channel and 2-channel CNN models were further modified and trained. The enface view of OCTA angiograms with different methods and inputs are presented and compared in Figure 6. One selected region consists of microvessel (marked with red line) is enlarged (zoomed in twice). It turns out that CNN is able to eliminate speckle noise, resulting in clean background and visually continuous vascular. Besides, CNN provides legible vessel outlines and presents much more details than SSAPGA, PID and CM.

In addition, the degrees of convergence are evaluated and plotted in Figure 6P. It shows that all of the models with different inputs have fast convergence due to batch normalization and ReLU. Apparently, the number of the inputs has a great impact on the performance of our CNN models, which is in line with conventional algorithms.

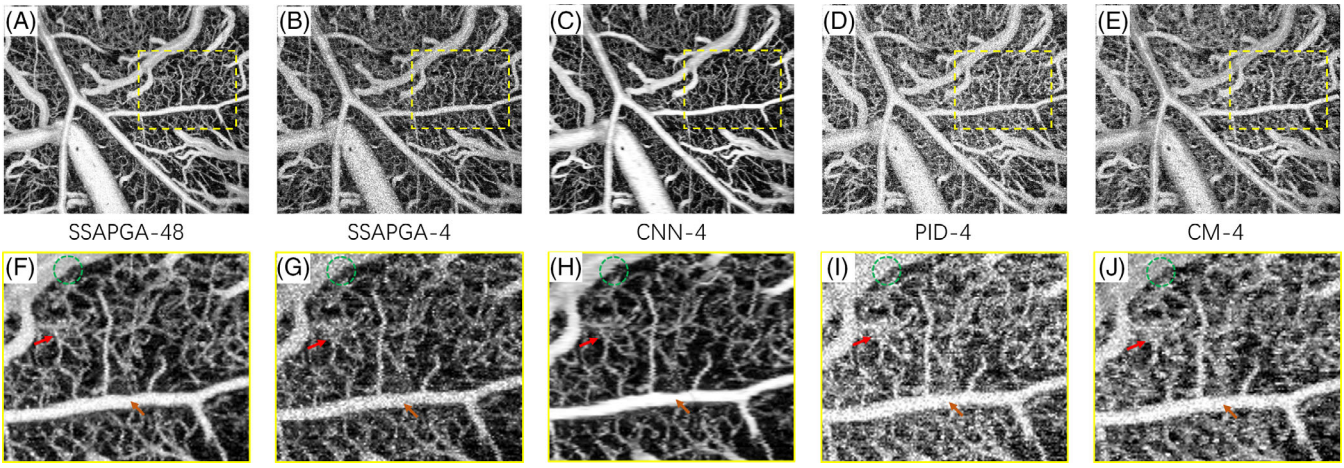

FIGURE 5 Enface optical coherence tomography angiography angiogram. A, Split-spectrum amplitude and phase-gradient angiography (SSAPGA) method with protocol of 48 consecutive scans at each slow-axis location; B-E, SSAPGA, convolutional neural network, power intensity differential and correlation mapping methods with protocol of four consecutive scans at each slow-axis location respectively. F-J, are enlarged images of selected regions, marked with yellow dotted lines

Quantitative analysis was conducted for comparison studies. We calculated the PSNR and structural similarity [49], which are commonly used in image to image translation tasks, between the predicted output and the ground truth. Quantitative analysis results of cross-sectional angiograms with different methods and protocols are presented in Table 1. As shown in the table, the CNN method is superior to the other methods with same scanning protocol. CM and PID present poor performance since they are sensitive to noise. Surprisingly, the performance of CNN method with two inputs outperforms SSAPGA with four inputs, which indicates great potentials of applying deep learning techniques to OCTA. The scanning time could be significantly reduced with good angiography performance.

Furthermore, we quantitatively compared enface MIP angiograms (size = 300×360) with different methods and protocols of the one testing volume after normalization. The results are shown in Table 2. As before, the CNN method demonstrates superior performance than the other methods.

One of the potential mechanisms of the deep learning model may be similar to the speckle-variance processing method, which measures decorrelation between the OCT signals generated by speckle or backscattered light from biological tissues. However, the deep learning model can further utilize the structural information and then eliminate speckle noise and background noise induced by OCTA imaging systems. Additionally, our label dataset is generated without any expert-labeling, which allows us to acquire a large amount of dataset for training. Therefore, our approach can be quickly applied to the other OCTA devices but avoiding from the possible influence of background noise induced by system nonlinearity. Additionally, this proposed pipeline has great potential in clinical use (ie, ophthalmology, dermatology).

However, there are still some limitations remained in this work. Each of the angiogram slide is not registered accurately, which raises the wavy artifacts along the slow axis. This is mainly caused by random galvanometer jitter, which is hard to correct. Another issue is that the intensity uniformity between angiogram slides is also influenced. Such issue is probably caused by the structure of our CNN model. Nevertheless, we believe these limitations can be solved by optimizing neural network and utilizing enface structural information.

4 | CONCLUSION

In this study, we propose a deep learning based pipeline as an alternative to conventional analytic OCTA algorithms. Benefiting from the powerful ability of data mining, our proposed CNN model can be trained to extract and analyze the OCT signal variation at different time points. Compare with the conventional methods, the image quality of cross-sectional angiogram is greatly improved with better SNR and speckle variance eliminating, resulting in further improvements in image quality and vessel connectivity of enface angiogram.

ACKNOWLEDGMENTS

This work was funded by the National Natural Science Foundation of China (81421004); the National Key Instrumentation Development Project of China (2013YQ030651) and the German Academic Exchange Service (GSSP57145465).

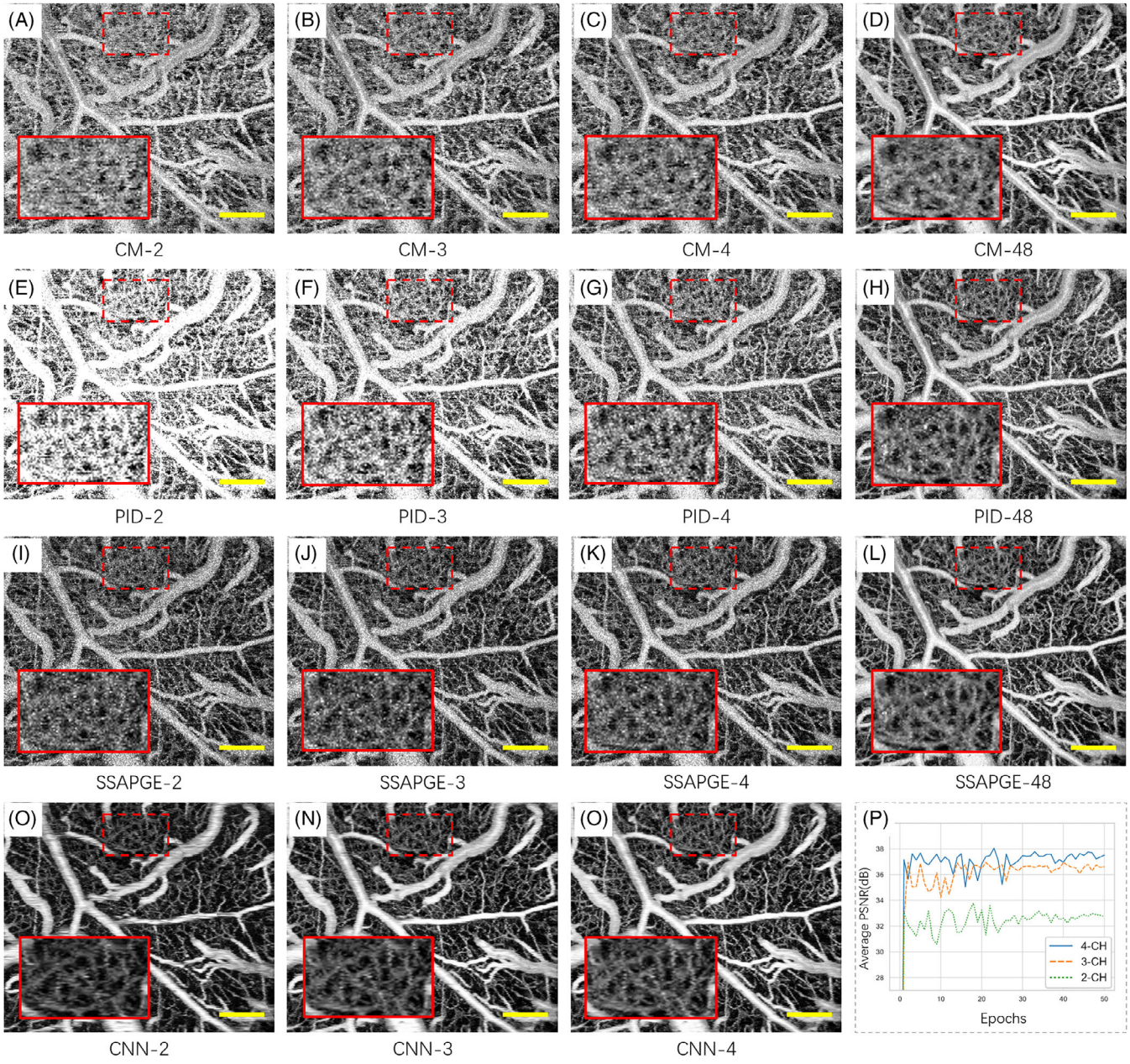

FIGURE 6 The enface view of optical coherence tomography angiography (OCTA) angiograms with different methods and inputs. A-O, En-face maximum intensity projection OCTA angiograms with different methods and scanning protocols. One selected region consists of microvessel (marked with red line) is enlarged and shown (zoomed in twice). P, Learning curves of the convolutional neural network model with three different protocols. The scale bar = 400 μm

	CM		PID		SSAPGA		CNN	
	PSNR	**SSIM**	**PSNR**	**SSIM**	**PSNR**	**SSIM**	**PSNR**	**SSIM**
4 inputs	18.95	0.24	18.90	0.22	20.79	0.69	**26.33**	**0.80**
3 inputs	18.56	0.22	17.94	0.18	19.69	0.64	**26.22**	**0.78**
2 inputs	17.60	0.18	16.29	0.13	18.49	0.56	**25.28**	**0.73**

TABLE 1 Average PSNR(dB)\SSIM results of the cross-sectional angiograms with different methods and protocols

Note: The best results are highlighted.

Abbreviations: CM, correlation mapping; CNN, convolutional neural network; PID, power intensity differential; PSNR, peak signal-to-noise ratio; SSAPGA, split-spectrum amplitude and phase-gradient angiography; SSIM, structural similarity.

TABLE 2 Quantitative comparison of the enface MIP angiograms with different methods and protocols

	CM		PID		SSAPGA		CNN	
	PSNR	**SSIM**	**PSNR**	**SSIM**	**PSNR**	**SSIM**	**PSNR**	**SSIM**
4 inputs	14.91	0.53	14.46	0.55	17.47	0.68	**19.65**	**0.78**
3 inputs	14.08	0.48	11.87	0.49	16.43	0.63	**18.63**	**0.74**
2 inputs	12.97	0.43	8.87	0.40	15.44	0.57	**16.03**	**0.63**

Note: The best results are highlighted.
Abbreviations: CM, correlation mapping; CNN, convolutional neural network; MIP, maximum intensity projection; PID, power intensity differential; PSNR, peak signal-to-noise ratio; SSAPGA, split-spectrum amplitude and phase-gradient angiography; SSIM, structural similarity.

Furthermore, we acknowledge the support of the NVIDIA Corporation with the donation of the Titan Xp GPU used for this research.

ORCID

Xi Liu https://orcid.org/0000-0003-1149-8951

REFERENCES

[1] D. Huang, E. A. Swanson, C. P. Lin, J. S. Schuman, W. G. Stinson, W. Chang, M. R. Hee, T. Flotte, K. Gregory, C. A. Puliafito, *Science (New York, NY)* **1991**, *254*, 1178.
[2] C. R. Baumal, *Curr. Opin. Ophthalmol.* **1999**, *10*, 182.
[3] P. H. Tomlins, R. Wang, *J. Phys. D Appl. Phys.* **2005**, *38*, 2519.
[4] W. Drexler, U. Morgner, F. Kärtner, C. Pitris, S. Boppart, X. Li, E. Ippen, J. Fujimoto, *Opt. Lett.* **1999**, *24*, 1221.
[5] J. Flammer, S. Orgül, V. P. Costa, N. Orzalesi, G. K. Krieglstein, L. M. Serra, J.-P. Renard, E. Stefánsson, *Prog. Retin. Eye Res.* **2002**, *21*, 359.
[6] E. Zagaynova, N. Gladkova, N. Shakhova, G. Gelikonov, V. Gelikonov, *J. Biophotonics* **2008**, *1*, 114.
[7] H. G. Bezerra, M. A. Costa, G. Guagliumi, A. M. Rollins, D. I. Simon, *J. Am. Coll. Cardiol. Intv.* **2009**, *2*, 1035.
[8] H.-P. Hammes, Y. Feng, F. Pfister, M. Brownlee, *Diabetes* **2011**, *60*, 9.
[9] E. C. Sattler, R. Kästle, J. Welzel, *J. Biomed. Opt.* **2013**, *18*, 061224.
[10] S. Dziennis, J. Qin, L. Shi, R. K. Wang, *Sci. Rep.* **2015**, *5*, 10051.
[11] E. Borrelli, E. H. Souied, K. B. Freund, G. Querques, A. Miere, O. Gal-Or, R. Sacconi, S. R. Sadda, D. Sarraf, *Retina* **2018**, *38*, 1968.
[12] D. Y. Kim, J. Fingler, J. S. Werner, D. M. Schwartz, S. E. Fraser, R. J. Zawadzki, *Biomed. Opt. Express* **2011**, *2*, 1504.
[13] Y. Yasuno, Y. Hong, S. Makita, M. Yamanari, M. Akiba, M. Miura, T. Yatagai, *Opt. Express* **2007**, *15*, 6121.
[14] J. Fingler, R. J. Zawadzki, J. S. Werner, D. Schwartz, S. E. Fraser, *Opt. Express* **2009**, *17*, 22190.
[15] Y. K. Tao, K. M. Kennedy, J. A. Izatt, *Opt. Express* **2009**, *17*, 4177.
[16] L. Yu, Z. Chen, *J. Biomed. Opt.* **2010**, *15*, 016029.
[17] S. S. Gao, Y. Jia, M. Zhang, J. P. Su, G. Liu, T. S. Hwang, S. T. Bailey, D. Huang, *Invest. Ophthalmol. Vis. Sci.* **2016**, *57*, OCT27.
[18] C. L. Chen, R. K. Wang, *Biomed. Opt. Express* **2017**, *8*, 1056.
[19] B. H. Park, M. C. Pierce, B. Cense, J. F. de Boer, *Opt. Express* **2003**, *11*, 782.
[20] V. X. Yang, M. L. Gordon, A. Mok, Y. Zhao, Z. Chen, R. S. Cobbold, B. C. Wilson, I. A. Vitkin, *Opt. Commun.* **2002**, *208*, 209.
[21] A. Mariampillai, B. A. Standish, E. H. Moriyama, M. Khurana, N. R. Munce, M. K. Leung, J. Jiang, A. Cable, B. C. Wilson, I. A. Vitkin, *Opt. Lett.* **2008**, *33*, 1530.
[22] Y. Jia, R. K. Wang, *J. Biophotonics* **2011**, *4*, 57.
[23] G. Liu, L. Chou, W. Jia, W. Qi, B. Choi, Z. Chen, *Opt. Express* **2011**, *19*, 11429.
[24] J. Tokayer, Y. Jia, A.-H. Dhalla, D. Huang, *Biomed. Opt. Express* **2013**, *4*, 1909.
[25] A. S. Nam, I. Chico-Calero, B. J. Vakoc, *Biomed. Opt. Express* **2014**, *5*, 3822.
[26] J. Enfield, E. Jonathan, M. Leahy, *Biomed. Opt. Express* **2011**, *2*, 1184.
[27] C. Blatter, J. Weingast, A. Alex, B. Grajciar, W. Wieser, W. Drexler, R. Huber, R. A. Leitgeb, *Biomed. Opt. Express* **2012**, *3*, 2636.
[28] S. B. Ploner, C. Riess, J. Schottenhamml, E. M. Moult, N. K. Waheed, J. G. Fujimoto, A. Maier in A Joint Probabilistic Model for Speckle Variance, Amplitude Decorrelation and Interframe Variance (IFV) Optical Coherence Tomography Angiography, Vol., Springer, **2018**, pp.98–102.
[29] K. He, X. Zhang, S. Ren, J. Sun, in Proc. of the IEEE Conf. on Computer Vision and Pattern Recognition, Las Vegas, NV, **2016**, p.770–778.
[30] O. Ronneberger, P. Fischer, T. Brox, in Int. Conf. on Medical Image Computing and Computer-Assisted Intervention, Auckland, New Zealand **2015**, p.234–241.
[31] K. Zhang, W. Zuo, Y. Chen, D. Meng, L. Zhang, *IEEE Trans. Image Process.* **2017**, *26*, 3142.
[32] Y. Lu, M. Kowarschik, X. Huang, Y. Xia, J. H. Choi, S. Chen, S. Hu, Q. Ren, R. Fahrig, J. Hornegger, *Med. Phys.* **2019**, *46*, 689.
[33] T. Würfl, M. Hoffmann, V. Christlein, K. Breininger, Y. Huang, M. Unberath, A. K. Maier, *IEEE Trans. Med. Imaging* **2018**, *37*, 1454.
[34] C. S. Lee, A. J. Tyring, Y. Wu, S. Xiao, A. S. Rokem, N. P. DeRuyter, Q. Zhang, A. Tufail, R. K. Wang, A. Y. Lee, *Scientific Reports.* **2019**, *9*, 5694.
[35] Z. Chen, T. E. Milner, S. Srinivas, X. Wang, A. Malekafzali, M. J. van Gemert, J. S. Nelson, *Opt. Lett.* **1997**, *22*, 1119.
[36] J. A. Izatt, M. D. Kulkarni, S. Yazdanfar, J. K. Barton, A. J. Welch, *Opt. Lett.* **1997**, *22*, 1439.

[37] S. Yazdanfar, A. M. Rollins, J. A. Izatt, *Opt. Lett.* **2000**, *25*, 1448.
[38] G. Liu, Y. Jia, A. D. Pechauer, R. Chandwani, D. Huang, *Biomed. Opt. Express* **2016**, *7*, 2943.
[39] A. Mariampillai, M. K. Leung, M. Jarvi, B. A. Standish, K. Lee, B. C. Wilson, A. Vitkin, V. X. Yang, *Opt. Lett.* **2010**, *35*, 1257.
[40] Y. Lu, M. Berger, M. Manhart, J.-h. Choi, M. Hoheisel, M. Kowarschik, R. Fahrig, Q. Ren, J. Hornegger, A. Maier, in IEEE 13th Int. Symp. on Biomedical Imaging (ISBI), **2016** p.457–460
[41] Y. Lecun, L. Bottou, Y. Bengio, P. Haffner, *Proc. IEEE.* **1998**, *86*, 2278.
[42] A. Krizhevsky, I. Sutskever, G. E. Hinton, in Advances in Neural Information Processing Systems Lake Tahoe, NV, **2012**, p.1097–1105.
[43] C. Szegedy, W. Liu, Y. Jia, P. Sermanet, S. Reed, D. Anguelov, D. Erhan, V. Vanhoucke, A. Rabinovich, in Proc. of the IEEE Conf. on Computer Vision and Pattern Recognition, Boston, MA **2015**, p.1–9.
[44] N. Srivastava, G. Hinton, A. Krizhevsky, I. Sutskever, R. Salakhutdinov, *J. Mach. Learn. Res.* **2014**, *15*, 1929.
[45] K. He, X. Zhang, S. Ren, J. Sun, in Proc. of the IEEE Int. Conf. on Computer Vision, Washington, DC **2015** p.1026–1034.
[46] D. P. Kingma, J. Ba, ICLR, San Diego, **2015**.
[47] S. Ioffe, C. Szegedy, ICML, JMLR.org, Lille, **2015**, p. 448.
[48] W. Luo, Y. Li, R. Urtasun, R. Zemel, in Advances in Neural Information Processing Systems, p.4898–4906.
[49] Z. Wang, A. C. Bovik, H. R. Sheikh, E. P. Simoncelli, *IEEE Trans. Image Process.* **2004**, *13*, 600.

How to cite this article: Liu X, Huang Z, Wang Z, et al. A deep learning based pipeline for optical coherence tomography angiography. *J. Biophotonics*. 2019;e201900008. https://doi.org/10.1002/jbio.201900008